


Two-particle tight-binding description of higher-harmonic generation in semiconductor nanostructures

Ulf Peschel ^{*}, Martin Thümmler, Thomas Lettau, and Stefanie Gräfe
Friedrich Schiller University Jena Max-Wien-Platz 1, 07743 Jena, Germany

Kurt Busch

Humboldt-Universität zu Berlin, AG Theoretische Optik & Photonik, Newtonstrasse 15, 12489 Berlin, Germany
and Max-Born-Institut, Max-Born-Straße 2A, 12489 Berlin, Germany



(Received 5 May 2022; revised 28 November 2022; accepted 5 December 2022; published 23 December 2022)

We develop a quantum mechanical theory to describe the optical response of semiconductor nanostructures with a particular emphasis on higher-order harmonic generation. Based on a tight-binding approach we take all two-particle correlations into account thus describing the creation, evolution, and annihilation of electrons and holes. In the limiting case of bulk materials, we obtain the same precision as that achieved by solving the well-established semiconductor Bloch equations. For semiconducting structures of finite extent, we also incorporate the surrounding space thus enabling a description of electron emission. In addition, we incorporate different relaxation mechanisms such as dephasing and damping of intraband currents. Starting from precise material data as, e.g., from tight-binding parameters obtained from density-functional-theory calculations, we obtain a numerical description being by far less computationally challenging and resource-demanding as comparable *ab initio* approaches, e.g., those based on time-dependent density functional theory.

DOI: [10.1103/PhysRevB.106.245307](https://doi.org/10.1103/PhysRevB.106.245307)

I. INTRODUCTION

Since the first observation of high-harmonic generation (HHG) in solids [1] it has become clear that its underlying physics is heavily determined by the band structure of the crystal lattice [2,3] resulting in interesting phenomena such as dynamical Bloch oscillations [4,5]. This complex electron-hole dynamics in dielectrics leaves its traces in the generated spectra [6,7]. Several theoretical approaches have been applied to describe this phenomenon, such as those based on the time-dependent Schrödinger equation (TDSE) [8] or time-dependent density-functional theory (TDDFT) [9]. In contrast to these computationally extremely challenging approaches, the semiconductor Bloch equations (SBEs) consider the full electron-hole evolution on the level of two-particle correlations [10,11] and have proven to be extremely successful with respect to the modeling of the bulk response. However, as SBEs are based on a Bloch-wave representation in reciprocal space, on first sight they appear to be unsuitable for a description of quantum systems with finite spatial extent.

Several attempts have been made to efficiently simulate HHG in nonperiodic semiconductor structures. Localized impurities have been studied based on a single-particle picture [12]. Explicit spatial dependencies have also to be considered to describe the effect of random lattice distortions [13,14]. The authors of those works utilized a Wannier-function based tight-binding description, which not only included single-particle transport, but also interband transitions. They could

demonstrate that the presence of random lattice distortions leads to HHG spectra with clean harmonic peaks, which otherwise can only be obtained for extremely short dephasing times in calculations based on SBEs. McDonald *et al.* have modeled HHG in semiconducting nanowires using a single-particle approach based on a frozen valence-band approximation [15]. They claimed that confinement may result in an effective enhancement mainly due to a change of the density of states. Very recently, CdSe semiconductor quantum dots have been experimentally examined in the context of HHG [16]. Surprisingly, HHG was found to be suppressed for smaller dots compared with the bulk material.

As of now, there is no theoretical method available which allows simulation and investigation of the nonlinear optical response of these quantum dots. Some insight can be obtained by solving a one-dimensional time-dependent Schrödinger equation (TDSE) for a single active electron (see Fig. 1 and the Appendix for details). It shows strong dynamical features induced by the optical pulse including partial electron emission, induced chaotic motion, and the generation of excited states by an optical pulse. For the smallest dots investigated here, the spectrum looks very noisy and featureless. The driven wave packet bounces off the potential wall, leading to a long living irregular motion. In real systems, damping removes such chaotic features, thus, helping to recover a clear spectrum. In the TDSE-based simulations, such damping can only be later artificially introduced by adding a time window to the signal prior to Fourier transformation (not done here). But regardless of the quality of generated spectra, TDSE-based simulations seem not to reproduce the experimental trend that HHG spectra decay faster for smaller than for larger

^{*}ulf.peschel@uni-jena.de

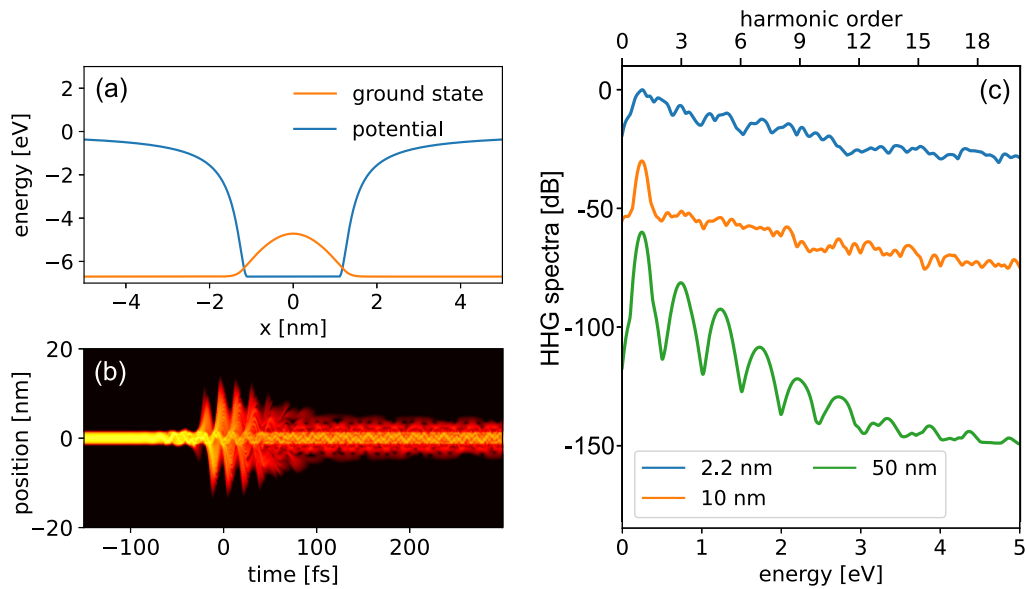


FIG. 1. Overview of the results obtained by solving the 1D time-dependent Schrödinger equation (TDSE) with a single active electron in a potential well. (a) Model potential with binding energy mimicking the work function of CdSe and ground state wave function for a small dot with a size of 2.2 nm. (b) Time-dependent electron density of the system driven by a laser field with a peak field strength of 2.5 V/nm. The electronic wave packet, which is initially in the ground state, remains excited, after the pulse has left. Small parts of the electronic wave function leave the dot and are partially driven back. (c) High-order harmonic spectrum from the TDSE model for dots of various sizes (graphs of the 10- and 50-nm dots are shifted downwards by 30 and 60 dB).

structures [16]. Hence, important features such as carrier generation and joint electron and hole dynamics, which are missing in a TDSE based simulation, seem to be essential to model HHG spectra of semiconductor nanostructures.

All those effects are in principle included in full real-time time-dependent density functional theory (rtTDDFT) simulations. We performed such calculations for nanostructures composed of 4, 16, and 64 atoms or 1, 4, and 16 unit cells of the underlying lattice, respectively, being exposed to a 50-fs pulse. We employed the package OCTOPUS ([17], see the Appendix for details) and it required more than 175 000 CPU hours of calculation for the 64-atom dot (see Fig. 2). To see significant HHG we had to increase the field strength to an unrealistically high value (10 V/nm instead of 2.5 V/nm). Still the resulting HHG spectra did not show the experimentally observed trend of a reduced efficiency for smaller structures, most likely because the simulated structures were much too small. Note that the smallest CdSe dots, for which HHG was observed in [16], consisted of about 170 unit cells corresponding to 680 atoms. For even smaller dots no significant HHG could be observed experimentally in certain agreement with our simulations. Hence, full *ab initio* approaches to HHG in dots are computationally prohibitive and other approaches are required.

In this work, we develop a quantum mechanical time-dependent tight-binding model for electrons and holes enabling us to describe of the optical response of semiconductor nanostructures such as, e.g., quantum dots or wires. To this end we transfer the SBEs from reciprocal to real space while keeping the same precision, at least for infinite structures. Such a perturbative approach results in two-particle wave functions describing the space-resolved generation and prop-

agation of electrons and holes. It also allows us to incorporate arbitrary semiconductor band structures that are obtained via density-functional theory (DFT) calculations. This tight-binding approach allows us to model interfaces as well as electron emission to the surrounding space. The derived equations lead to computationally efficient codes, allowing us to simulate the nonlinear optical response of semiconducting nanostructures on a conventional laptop computer.

Here, we illustrate the basic features of the general theory for the simplest case. We restrict ourselves to a one-dimensional two-band description, considering only a single valence and a single conduction band. Although the actual 3D structure of, e.g., a real semiconductor wire or even a dot is not adequately reflected by this treatment, it is straightforward to extend our approach to three dimensions and any semiconductor having (usually) more relevant valence bands.

The paper is structured as follows: We first define the basis of our tight-binding approach by discussing the single-particle system in the bulk. Then, we perform a second quantization towards a many-particle description. Starting from electron and hole creation and annihilation operators in reciprocal space, we derive the tight-binding Hamiltonian of the semiconductor in second quantization including light-matter interaction. As electrons may leave the nanostructure, we also include the space surrounding the dot into our approach. With the complete Hamiltonian in our hands, we then proceed to define the optical polarization and formulate a set of coupled differential equations for its evolution. Finally, we apply the scheme to our model system that resembles a CdSe quantum nanostructure. A summary concludes the paper, and a collection of material properties and numerical parameters can be found in the Appendix.

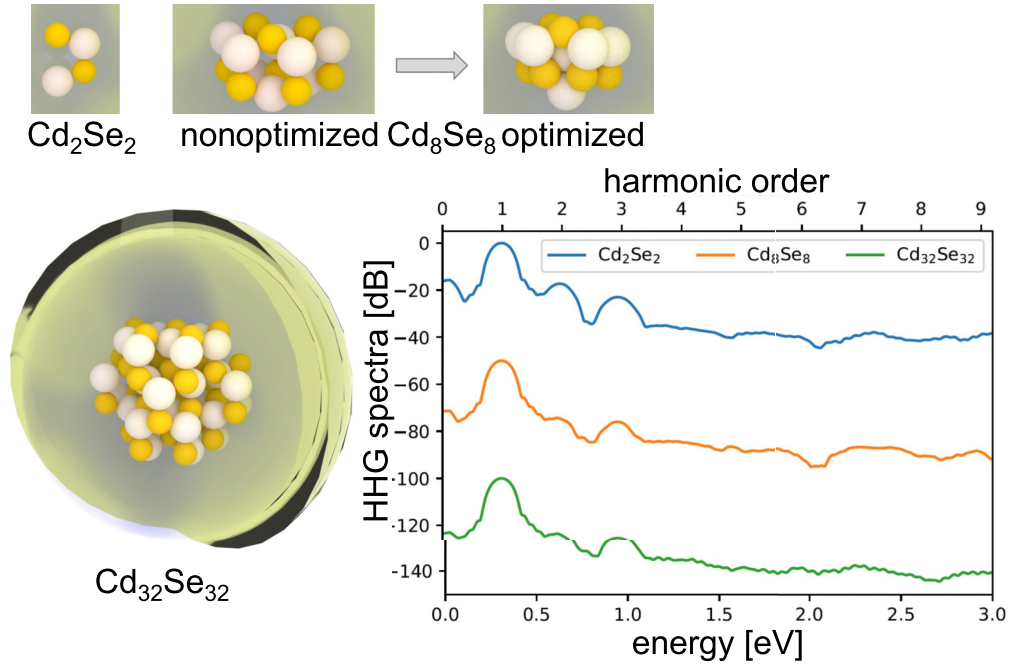


FIG. 2. HHG spectra of CdSe clusters calculated with rtTDDFT using an excitation pulse with peak field strength of 9.95 V/nm and 50 fs duration to reduce computation time. Clusters were optimized for minimum equilibrium energy. For the largest possible structure ($\text{Cd}_{32}\text{Se}_{32}$), the spherical simulation box including the absorber is shown.

II. SINGLE-PARTICLE SYSTEM IN THE BULK

A. Eigenfunctions and eigenenergies

All formulas are expressed in atomic units, i.e., we set $e = 1$, $\hbar = 1$, $m_e = 1$, $\epsilon_0 = 1$, and we restrict ourselves to a one-dimensional representation (for a straightforward generalization towards three dimensions see, e.g., Ref. [18] and references therein).

We start from the single particle eigenfunctions of the unperturbed bulk crystal. In the real-space representation, the corresponding Bloch waves $|\psi_k^\eta\rangle$ of a certain band η and Bloch vector $k - \frac{\pi}{a} \leq k \leq \frac{\pi}{a}$ read as

$$\langle x | \psi_k^\eta \rangle = \psi_k^\eta(x) = u_k^\eta(x) \exp(ikx), \quad (1)$$

where $u_k^\eta(x)$ is the lattice periodic part $u_k^\eta(x+a) = u_k^\eta(x)$ and a denotes the size of the elementary cell. These Bloch waves $|\psi_k^\eta\rangle$ fulfill the orthogonality relation

$$\langle \psi_{k'}^{\eta'} | \psi_k^\eta \rangle = \int_{-\infty}^{\infty} dx \psi_{k'}^{\eta'}(\vec{r})^* \psi_k^\eta(\vec{r}) = \delta_{\eta\eta'} \delta(k-k'), \quad (2)$$

where $\delta_{\eta\eta'}$ is the Kronecker symbol and $\delta(k-k')$ is the delta distribution.

Their phase can be chosen such that the symmetry relation $u_{-k}^\eta(x) = u_k^\eta(x)^*$ is fulfilled. The energies $\epsilon_\eta(k)$ are eigenvalues of the single-particle Hamiltonian $\hat{\mathbf{H}}_0$, i.e.,

$$\hat{\mathbf{H}}_0 |\psi_k^\eta\rangle = \epsilon_\eta(k) |\psi_k^\eta\rangle, \quad (3)$$

and have the Fourier expansion

$$\epsilon_\eta(k) = \sum_{m=-\infty}^{\infty} \epsilon_m^\eta \exp(imak). \quad (4)$$

As the band structure is symmetric and real, $\epsilon_m^\eta = \epsilon_m^{\eta*} = \epsilon_{-m}^\eta$ holds. For the considered case of a dielectric with direct transition at $k=0$, there is a gap in the energy spectrum defined as $\epsilon_{\text{gap}} = \sum_{m=-\infty}^{\infty} (\epsilon_m^c - \epsilon_m^v)$. In what follows, we consider a two-band model and define the energy zero in the middle of the gap between the valence and the conduction band.

The Fourier coefficients of the bands are related to the experimentally well-accessible effective masses given by $\frac{1}{m_\eta} = \frac{\partial^2}{\partial k^2} \epsilon_\eta(k) |_{k=0} = -2 \sum_{m=1}^{\infty} (ma)^2 \epsilon_m^\eta$. Restricting ourselves to the zeroth and the first Fourier component, we obtain within the two-band model a cosine-shaped band structure as $\epsilon_\eta(k) \approx \frac{\epsilon_{\text{gap}}}{2} - \frac{1}{m_\eta a^2} \cos(ak)$, which will allow us later to restrict to nearest neighbor interactions.

B. Transition dipole elements between conduction and valence band

The transition dipole matrix elements between the conduction and valence band are

$$D(k) = \int_{-a/2}^{a/2} dx u_k^{c*}(x) x u_k^v(x), \quad (5)$$

with the Fourier expansion

$$D(k) = \sum_{m=-\infty}^{\infty} D_m \exp(imak), \quad (6)$$

and $D_{-m} = D_m^*$ caused by time-inversion symmetry of the Bloch waves [see the phase choice with respect of an inversion of k discussed below Eq. (2)].

Note that the above definition (5) is rarely used because of the ambiguity of the definition of the elementary cell in a periodic lattice. In DFT calculations one usually determines respective momentum elements first which are later used to derive the required dipole elements (for a detailed discussion see [19,20]). But this has no effect on the Fourier expansion (6) and the resulting symmetries.

We again restrict to the simplest case $m = 0$, i.e., a completely local optical transition without any immediate transverse transport.

C. Tight-binding approach

A maximally localized or Wannier state $|\varphi_n^\eta\rangle$ of band η on site n is constructed by a superposition of Bloch waves and reads in spatial representation as

$$\begin{aligned} \langle x|\varphi_n^\eta\rangle &= \varphi_n^\eta(x) = \sqrt{\frac{a}{2\pi}} \int_{-\pi/a}^{\pi/a} dk \psi_k^\eta(x+na) \\ &= \sqrt{\frac{a}{2\pi}} \int_{-\pi/a}^{\pi/a} dk u_k^\eta(x) \exp[ik(x+na)], \end{aligned} \quad (7)$$

where the phase of the Bloch waves is chosen such that maximum localization of the tight-binding states $\varphi_n^\eta(x)$ is obtained. As Bloch waves and Wannier states are connected by a unitary transformation, the Wannier functions obey the orthogonality relation

$$\int_{-\infty}^{\infty} dx \varphi_{n'}^\eta(x)^* \varphi_n^\eta(x) = \delta_{\eta'\eta} \delta_{nm'}. \quad (8)$$

Different tight-binding states are solely shifted with respect to each other by multiples of the lattice period according to

$$\begin{aligned} \varphi_{n+m}^\eta(x) &= \int_{-\pi/a}^{\pi/a} dk u_k^\eta(x) \exp[ik(x+na+ma)] \\ &= \varphi_n^\eta(x+ma). \end{aligned} \quad (9)$$

III. MANY-PARTICLE APPROACH

A. Electron creation and annihilation operators of Bloch states

In the equilibrium state $|0\rangle$ of the system, thermal excitations of conduction-band electrons can be neglected. Hence, initially all single-particle states of the valence band are occupied by electrons and all conduction-band states are empty. The creation of an electron with a certain quasimomentum k in state $|\psi_k^c\rangle$ of the conduction band is described by the creation operator $\hat{\Psi}_k^{c+}$. It is accompanied by the removal of an electron from the valence band, a process which is described by the application of a fermionic annihilation operator $\hat{\Psi}_k^v$. Here, we have already assumed that momentum conservation holds which is typical for optical excitations. The resulting creation of an excited state $|*\rangle_k$ is thus expressed as $|*\rangle_k = \hat{\Psi}_k^{c+} \hat{\Psi}_k^v |0\rangle$.

Those creation and annihilation operators are adjoint to each other $\hat{\Psi}_k^{\eta+} = (\hat{\Psi}_k^\eta)^\dagger$ and obey the anticommutator $[\hat{\mathbf{A}}, \hat{\mathbf{B}}]_+ = \hat{\mathbf{A}}\hat{\mathbf{B}} + \hat{\mathbf{B}}\hat{\mathbf{A}}$ relations $[\hat{\Psi}_k^\eta, \hat{\Psi}_{k'}^{\eta'+}]_+ = [\hat{\Psi}_k^{\eta+}, \hat{\Psi}_{k'}^{\eta'+}]_+ = 0$ and $[\hat{\Psi}_k^\eta, \hat{\Psi}_{k'}^{\eta'+}]_+ = \hat{\Psi}_k^\eta \hat{\Psi}_{k'}^{\eta'+} + \hat{\Psi}_{k'}^{\eta'+} \hat{\Psi}_k^\eta = \delta_{\eta\eta'} \delta(k-k')$, where the number operator $\hat{\Psi}_k^{\eta+} \hat{\Psi}_k^\eta$ appears.

B. Introduction of holes

It is convenient to rather count holes instead of electrons in the valence band. Hence, new electron and hole creation and annihilation operators are introduced as $\hat{\Psi}_k^v = \hat{\mathbf{h}}_{-k}^+$ and $\hat{\Psi}_k^{c+} = \hat{\mathbf{e}}_k^+$ and the momentum conserving creation of an electron-hole pair now reads as $|*\rangle_k = \hat{\mathbf{e}}_k^+ \hat{\mathbf{h}}_{-k}^+ |0\rangle$.

While anticommutator relations and conduction band energies remain unchanged, hole energies feature a sign change as compared with valence band energies, i.e., while $\varepsilon_e(k) = \varepsilon_c(k)$ it is $\varepsilon_h(k) = -\varepsilon_v(k)$.

C. Many-particle Hamiltonian of the bulk solid in the Bloch basis

The simplest form of the bulk many-particle Hamiltonian in the Bloch-wave basis within our approximations (two band model, one-dimensional description, no Coulomb interaction) reads as

$$\hat{\mathbf{H}}^B = \hat{\mathbf{H}}_0^B + \hat{\mathbf{H}}_{\text{inter}}^B + \hat{\mathbf{H}}_{\text{intra}}^B. \quad (10)$$

$\hat{\mathbf{H}}_0^B$ accounts for the energies of the bulk semiconductor as defined in (3) and, in terms of creation and annihilation operators, read as

$$\hat{\mathbf{H}}_0^B = \int_{-\pi/a}^{\pi/a} dk [\varepsilon_e(k) \hat{\mathbf{e}}_k^+ \hat{\mathbf{e}}_k + \varepsilon_h(k) \hat{\mathbf{h}}_k^+ \hat{\mathbf{h}}_k]. \quad (11)$$

$\hat{\mathbf{H}}_{\text{inter}}^B$ describes the optical transitions between bands under the action of a time-dependent electrical field $E(t)$ as

$$\hat{\mathbf{H}}_{\text{inter}}^B = E(t) \int_{-\pi/a}^{\pi/a} dk [D(k) \hat{\mathbf{e}}_k^+ \hat{\mathbf{h}}_{-k}^+ + D(k)^* \hat{\mathbf{h}}_{-k} \hat{\mathbf{e}}_k]. \quad (12)$$

The optical field also accelerates charge carriers within their respective bands, an effect which is represented by

$$\hat{\mathbf{H}}_{\text{intra}}^B = iE(t) \int_{-\pi/a}^{\pi/a} dk \left(\hat{\mathbf{e}}_k^+ \frac{\partial}{\partial k} \hat{\mathbf{e}}_k - \hat{\mathbf{h}}_k^+ \frac{\partial}{\partial k} \hat{\mathbf{h}}_k \right). \quad (13)$$

The Hamiltonian introduced in (10) leads to the well-known SBEs [10,11]. In what follows, we will refrain from using this Hamiltonian directly, but rather will apply a tight-binding approach which will lead to evolution equations that are as accurate as the SBEs when it comes to the description of the bulk.

D. Tight-binding approach

Tight-binding creation and annihilation operators of electrons and holes are derived from respective operators in the Bloch basis using the unitary transformation (7), similar to what has been done for the single-particle wave functions:

$$\begin{aligned} \hat{\mathbf{e}}_n &= \sqrt{\frac{a}{2\pi}} \int_{-\pi/a}^{\pi/a} dk \hat{\mathbf{e}}_k \exp(ikna) \\ \text{and } \hat{\mathbf{h}}_n &= \sqrt{\frac{a}{2\pi}} \int_{-\pi/a}^{\pi/a} dk \hat{\mathbf{h}}_k \exp(ikna). \end{aligned} \quad (14)$$

The associated inverse transformation

$$\hat{\mathbf{e}}_k = \sqrt{\frac{a}{2\pi}} \sum_n \hat{\mathbf{e}}_n \exp[-ikna]$$

and $\hat{\mathbf{h}}_k = \sqrt{\frac{a}{2\pi}} \sum_n \hat{\mathbf{h}}_n \exp[-ikna]$, (15)

is based on the relation $\sum_n \exp(inka) = \frac{2\pi}{a} \delta(k)$ for $-\frac{\pi}{a} < k \leq \frac{\pi}{a}$. Again, creation and annihilation operators are adjoint counterparts, i.e., $\hat{\mathbf{e}}_n^+ = (\hat{\mathbf{e}}_n)^+$ and $\hat{\mathbf{h}}_n^+ = (\hat{\mathbf{h}}_n)^+$. Hence, an excited state $|*\rangle_n$ consisting of, e.g., an electron and a hole at site n is created from the equilibrium state by applying the corresponding creation operators $|*\rangle_n = \hat{\mathbf{e}}_n^+ \hat{\mathbf{h}}_n^+ |0\rangle$.

As the above transformation is unitary, respective anticommutator and orthogonality relations result in

$$[\hat{\mathbf{e}}_n, \hat{\mathbf{e}}_{n'}]_+ = [\hat{\mathbf{h}}_n, \hat{\mathbf{h}}_{n'}]_+ = [\hat{\mathbf{e}}_n, \hat{\mathbf{h}}_{n'}]_+ = [\hat{\mathbf{e}}_n, \hat{\mathbf{h}}_n^+]_+ = 0$$

$$\text{and } [\hat{\mathbf{e}}_n, \hat{\mathbf{e}}_{n'}^+]_+ = \delta_{nn'}, \quad [\hat{\mathbf{h}}_n, \hat{\mathbf{h}}_{n'}^+]_+ = \delta_{nn'}, \quad (16)$$

ensuring fermionic properties. The operators $\hat{\mathbf{N}}_n^e = \hat{\mathbf{e}}_n^+ \hat{\mathbf{e}}_n$ and $\hat{\mathbf{N}}_n^h = \hat{\mathbf{h}}_n^+ \hat{\mathbf{h}}_n$ now count electrons and holes on site n , respectively. Their expectation values evaluate to 0 and 1 if applied to the ground $|0\rangle$ and the set of excited states $|*\rangle_n$, respectively.

IV. MANY-PARTICLE HAMILTONIAN OF THE BULK SOLID IN THE TIGHT-BINDING BASIS

Inserting the inverse unitary transformation (15) into $\hat{\mathbf{H}}_0^B$ defined in Eq. (11) and using the Fourier expansion of the single particle energies (4) results in

$$\hat{\mathbf{H}}_0^{tb} = \sum_{n=-\infty}^{\infty} \sum_{m=-\infty}^{\infty} (\varepsilon_m^e \hat{\mathbf{e}}_n^+ \hat{\mathbf{e}}_{n-m} + \varepsilon_m^h \hat{\mathbf{h}}_n^+ \hat{\mathbf{h}}_{n-m}). \quad (17)$$

Note that all higher Fourier terms $|m| \geq 1$ account for particle hopping between the sides.

In what follows we restrict to nearest neighbor interaction and use the tight-binding Hamiltonian

$$\begin{aligned} \hat{\mathbf{H}}_0^{tb} = & \sum_{n=-\infty}^{\infty} \left[\frac{\varepsilon_{\text{gap}}}{2} (\hat{\mathbf{e}}_n^+ \hat{\mathbf{e}}_n + \hat{\mathbf{h}}_n^+ \hat{\mathbf{h}}_n) \right. \\ & - \frac{1}{2m_e a^2} (\hat{\mathbf{e}}_{n+1}^+ \hat{\mathbf{e}}_n + \hat{\mathbf{e}}_n^+ \hat{\mathbf{e}}_{n+1} - \hat{\mathbf{e}}_n^+ \hat{\mathbf{e}}_n - \hat{\mathbf{e}}_{n+1}^+ \hat{\mathbf{e}}_{n+1}) \\ & \left. \times - \frac{1}{2m_h a^2} (\hat{\mathbf{h}}_{n+1}^+ \hat{\mathbf{h}}_n + \hat{\mathbf{h}}_n^+ \hat{\mathbf{h}}_{n+1} - \hat{\mathbf{h}}_n^+ \hat{\mathbf{h}}_n - \hat{\mathbf{h}}_{n+1}^+ \hat{\mathbf{h}}_{n+1}) \right] \end{aligned} \quad (18)$$

with $\varepsilon_{\text{gap}} = \varepsilon_0^e + \varepsilon_1^e + \varepsilon_0^h + \varepsilon_1^h$.

We now apply the same procedure to the interband transitions, Eq. (12), and employ the Fourier decomposition of the dipole matrix elements, Eq. (6), resulting in

$$\begin{aligned} \hat{\mathbf{H}}_{\text{inter}}^{tb} = & E(t) \sum_{n=-\infty}^{\infty} \left\{ D_0 \hat{\mathbf{e}}_n^+ \hat{\mathbf{h}}_n^+ + \sum_{m=1}^{\infty} [\text{Re}(D_m) \hat{\mathbf{e}}_n^+ (\hat{\mathbf{h}}_{n+m}^+ + \hat{\mathbf{h}}_{n-m}^+) \right. \\ & \left. - i \text{Im}(D_m) \hat{\mathbf{e}}_n^+ (\hat{\mathbf{h}}_{n+m}^+ - \hat{\mathbf{h}}_{n-m}^+) \right\} + \text{H.c.}, \end{aligned} \quad (19)$$

where H.c. denotes the Hermitian conjugate. Hence, upon an optical excitation, a k -dependent dipole matrix element causes transverse transport. Such transport can be symmetric in the case of a real dipole element or may have an antisymmetric component for a nonvanishing imaginary part.

As a further assumption, we restrict ourselves to spatially local transitions using an interband Hamiltonian as

$$\hat{\mathbf{H}}_{\text{inter}}^{tb} = E(t) D_0 \sum_{n=-\infty}^{\infty} (\hat{\mathbf{e}}_n^+ \hat{\mathbf{h}}_n^+ + \hat{\mathbf{h}}_n \hat{\mathbf{e}}_n). \quad (20)$$

Applying the inverse unitary transformation to $\hat{\mathbf{H}}_{\text{inter}}^{tb}$ yields within the dipole approximation

$$\hat{\mathbf{H}}_{\text{intra}}^{tb} = -E(t) \sum_{n=-\infty}^{\infty} a n (\hat{\mathbf{h}}_n^+ \hat{\mathbf{h}}_n - \hat{\mathbf{e}}_n^+ \hat{\mathbf{e}}_n). \quad (21)$$

V. MANY-PARTICLE HAMILTONIAN FOR A SEMICONDUCTOR NANOSTRUCTURE

Now, we discuss the interaction of a strong optical field with a confined system, a quantum wire or dot centered at position x_0 . It is assumed to consist of semiconducting material in a range $|x - x_0| \leq L/2$, which is embedded in free space, either vacuum or a material without any crystalline structure, e.g., a liquid.

A. Tight-binding description of electron motion

As electrons might be able to leave the nanostructure due to the acceleration by the optical field, we have to describe the surrounding space in a manner consistent with the tight-binding description of the semiconductor. Although the free space outside is continuous, any numerical procedure requires its discretization to successfully describe the motion of a quantum particle within it. Hence, a tight-binding description is justified also for free space as long as spatial phase variations are described correctly, at least for relevant values of momenta.

We again start with the single-particle Hamiltonian of the electron in free space. To account for the ionization energy each electron emitted into free space is labeled with a rest energy $\varepsilon_{\text{free space}}$ as measured from the middle of the gap of the semiconductor. Within a numerical description, free space will be discretized in a regular lattice with a spacing of dx as

$$\begin{aligned} \hat{\mathbf{H}}_0^f = & \int_{\text{free space}} dx \left[\varepsilon_{\text{free space}} \psi(x)^* \psi(x) \right. \\ & \left. + \psi(x)^* \left(-\frac{1}{2} \frac{\partial^2}{\partial x^2} \right) \psi(x) \right] \\ \approx & \sum_n^{\text{free space}} \left[\varepsilon_{\text{free space}} \sqrt{dx} \psi(n dx)^* \sqrt{dx} \psi(n dx) \right. \\ & - \sqrt{dx} \psi(n dx)^* \frac{1}{2 dx^2} \{ \sqrt{dx} \psi[(n+1) dx] \\ & \left. + \sqrt{dx} \psi[(n-1) dx] - 2\sqrt{dx} \psi(n dx) \} \right]. \end{aligned}$$

Accordingly, in the above Hamiltonian we have replaced the continuous single-particle wave function $\psi(x)$

by a discrete set of complex amplitudes $\sqrt{dx} \psi(n dx)$ and $\sqrt{dx} \psi(n dx)^*$. Following the scheme of second quantization these amplitudes are replaced by electron annihilation \hat{e}_n and creation operators \hat{e}_n^+ where the normalization is chosen such that $\hat{e}_n^+ \hat{e}_n$ counts the number of electrons in the space interval $(n - \frac{1}{2}) dx < x \leq (n + \frac{1}{2}) dx$. This results in a free-space tight-binding Hamiltonian with discretized spatial derivative as

$$\hat{H}_0^f = \sum_n^{\text{free space}} \left[\varepsilon_{\text{free space}} \hat{e}_n^+ \hat{e}_n - \frac{1}{2 dx^2} (\hat{e}_n^+ \hat{e}_{n+1} + \hat{e}_{n+1}^+ \hat{e}_n - \hat{e}_n^+ \hat{e}_n - \hat{e}_{n+1}^+ \hat{e}_{n+1}) \right]. \quad (22)$$

Hence, within a tight-binding approximation, electrons in free space and in the conduction band of a semiconductor are described in a very similar fashion [compare Eqs. (18) and (22)].

As for every numerical description, accumulated phase differences between neighboring sites must remain much smaller than π . Hence, the higher the momenta acquired by electrons outside the nanostructure, the finer the discretization (here dx) must be.

In what follows we will combine bulk (18) and free space (22) versions into a global Hamiltonian

$$\hat{H}_0 = \sum_{n=-\infty}^{\infty} \left[\varepsilon_n^e \hat{e}_n^+ \hat{e}_n + \varepsilon_n^h \hat{h}_n^+ \hat{h}_n - c_n^e (\hat{e}_{n+1}^+ \hat{e}_n + \hat{e}_n^+ \hat{e}_{n+1} - \hat{e}_n^+ \hat{e}_n - \hat{e}_{n+1}^+ \hat{e}_{n+1}) - c_n^h (\hat{h}_{n+1}^+ \hat{h}_n + \hat{h}_n^+ \hat{h}_{n+1} - \hat{h}_n^+ \hat{h}_n + \hat{h}_{n+1}^+ \hat{h}_{n+1}) \right] \quad (23)$$

with a space dependent electron energy

$$\varepsilon_n^e = \begin{cases} \frac{\varepsilon_g}{2} & \text{inside the nanostructure for } |na - x_0| \leq L/2 \\ \varepsilon_{\text{free space}} & \text{in free space} \end{cases}.$$

The coupling constants of electrons c_n^e between sites n and $n + 1$ are also spatially dependent, according to

$$c_n^e = \begin{cases} \frac{1}{2a^2 m_e} & \text{inside the nanostructure for } |na - x_0| \leq L/2 \\ \frac{1}{2 dx^2} & \text{in free space} \end{cases}.$$

In contrast, holes cannot enter free space, resulting in a vanishing coupling outside the nanostructure, thus

$$c_n^h = \begin{cases} \frac{1}{2a^2 m_h} & \text{inside the nanostructure for } |na - x_0| \leq L/2 \\ 0 & \text{in free space} \end{cases}.$$

Although such treatment allows for a consistent description of semiconductor nanostructures in their respective environment, surface states might not be reproduced correctly and, therefore, for realistic applications of our framework, further modification of tight-binding parameters close to the interface might be required.

B. Optical field action in the nanostructure and free space

Optical transitions can only happen inside the semiconductor. Therefore, $\hat{H}_{\text{intra}}^{tb}$ in Eq. (20) does not need any

modification except for setting the transition dipole matrix element to zero outside, resulting in

$$\hat{H}_{\text{inter}} = E(t) \sum_{n=-\infty}^{\infty} d_n (\hat{e}_n^+ \hat{h}_n^+ + \hat{h}_n \hat{e}_n) \quad (24)$$

with

$$d_n = \begin{cases} D_0 & \text{inside the nanostructure for } |na - x_0| \leq L/2 \\ 0 & \text{in free space} \end{cases}$$

Electrons in free space are accelerated by the optical field. Hence, $\hat{H}_{\text{intra}}^{tb}$ of Eq. (21) needs to be modified in order to include near-field effects as

$$\hat{H}_{\text{intra}} = E(t) \sum_{n=-\infty}^{\infty} V_n (\hat{h}_n^+ \hat{h}_n - \hat{e}_n^+ \hat{e}_n). \quad (25)$$

This incorporates a spatially inhomogeneous and time-dependent effective potential $E(t)V_n$. In a quasistatic approximation, the time-dependent electric field $E(t)$ is combined with a spatially varying factor V_n that accounts for local field enhancements. We assume that the overall nonlinear response is weak and that the spatial shape of the optical driving field is still determined by the linear optical response of the structure.

To demonstrate the effects of spatial dependence of the incidence field, we approximate the optical field around the ends of the nanostructure by that occurring around a dielectric sphere centered at x_0 , for which analytical expressions are known for the static case [21],

$$V_n = - \left(\frac{3 \varepsilon_{\text{free space}}^R}{\varepsilon_{\text{bulk}}^R + 2 \varepsilon_{\text{free space}}^R} \right) \times (na - x_0) \quad \text{inside the nanostructure,}$$

$$V_n = -(na - x_0) + \left(\frac{\varepsilon_{\text{bulk}}^R - \varepsilon_{\text{free space}}^R}{\varepsilon_{\text{bulk}}^R + 2 \varepsilon_{\text{free space}}^R} \right) \times \frac{(L/2)^3}{|na - x_0|^3} (na - x_0) \quad \text{in free space.} \quad (26)$$

In the above expressions, we denote with $\varepsilon_{\text{bulk}}^R$ and $\varepsilon_{\text{free space}}^R$, respectively, the relative dielectric constants of the semiconductor material and of the surrounding space at the frequency of the incident light field.

C. Condensed notation of the Hamiltonian

Taken together, the Hamiltonian $\hat{H} = \hat{H}_0 + \hat{H}_{\text{inter}} + \hat{H}_{\text{intra}}$ can be summarized as

$$\hat{H} = \sum_{n=-\infty}^{\infty} \left[\tilde{\varepsilon}_n^e \hat{e}_n^+ \hat{e}_n + \tilde{\varepsilon}_n^h \hat{h}_n^+ \hat{h}_n + d_n E(t) (\hat{e}_n^+ \hat{h}_n^+ + \hat{h}_n \hat{e}_n) - c_n^e (\hat{e}_{n+1}^+ \hat{e}_n + \hat{e}_n^+ \hat{e}_{n+1}) - c_n^h (\hat{h}_{n+1}^+ \hat{h}_n + \hat{h}_n^+ \hat{h}_{n+1}) \right], \quad (27)$$

where we have introduced time- and space-dependent electron $\tilde{\varepsilon}_n^e(t) = \varepsilon_n^e + c_{n-1}^e + c_n^e - E(t)V_n$ and hole energies $\tilde{\varepsilon}_n^h(t) = \varepsilon_n^h + c_{n-1}^h + c_n^h + E(t)V_n$ to simplify the notation for the subsequent derivation of the evolution equation of the polarization.

VI. EVOLUTION OF POLARIZATION AND CURRENT WITHIN THE TIGHT-BINDING APPROXIMATION

A. Definition of the polarization and currents interacting with the optical field

In a classical Hamiltonian description, light-matter interaction is represented by the term $\sim \vec{P}\vec{E}$ formed by a product of the field and polarization. Hence, we can immediately identify the operator of the optical polarization by collecting all the terms that contain the electric field. It follows from (24) and (25) that the total polarization is

$$\hat{\mathbf{P}} = \sum_{n=-\infty}^{\infty} [d_n(\hat{\mathbf{e}}_n^+\hat{\mathbf{h}}_n^+ + \hat{\mathbf{h}}_n\hat{\mathbf{e}}_n) + V_n(\hat{\mathbf{h}}_n^+\hat{\mathbf{h}}_n - \hat{\mathbf{e}}_n^+\hat{\mathbf{e}}_n)]. \quad (28)$$

It contains the non-Hermitian interband polarizations $d_n\hat{\mathbf{h}}_n^+\hat{\mathbf{e}}_n$ on a site n and the polarization due to charge imbalances $V_n(\hat{\mathbf{h}}_n^+\hat{\mathbf{h}}_n - \hat{\mathbf{e}}_n^+\hat{\mathbf{e}}_n)$ induced by macroscopic currents. The latter term is particularly relevant in nanostructures when charge imbalances accumulate close to the interface.

B. Evolution equations of operators

In order to determine the optical polarization within the Heisenberg picture, we first use the Schrödinger equation to derive evolution equations for creation and annihilation operators based on the Hamiltonian $\hat{\mathbf{H}}$ displayed in Eq. (27) as

$$\begin{aligned} i\frac{d}{dt}\hat{\mathbf{e}}_n &= [\hat{\mathbf{e}}_n, \hat{\mathbf{H}}] = \hat{\mathbf{e}}_n\hat{\mathbf{H}} - \hat{\mathbf{H}}\hat{\mathbf{e}}_n = \tilde{\varepsilon}_n^e\hat{\mathbf{e}}_n - c_{n-1}^e\hat{\mathbf{e}}_{n-1} - c_n^e\hat{\mathbf{e}}_{n+1} + E(t)d_n\hat{\mathbf{h}}_n^+, \\ i\frac{d}{dt}\hat{\mathbf{h}}_n &= [\hat{\mathbf{h}}_n, \hat{\mathbf{H}}] = \hat{\mathbf{h}}_n\hat{\mathbf{H}} - \hat{\mathbf{H}}\hat{\mathbf{h}}_n = \tilde{\varepsilon}_n^h\hat{\mathbf{h}}_n - c_{n-1}^h\hat{\mathbf{h}}_{n-1} - c_n^h\hat{\mathbf{h}}_{n+1} - E(t)d_n\hat{\mathbf{e}}_n^+. \end{aligned} \quad (32)$$

All operators on site n are coupled to those from neighboring sites. Therefore, all two-particle operators $\hat{\mathbf{n}}_{nm}^e = \hat{\mathbf{e}}_n^+\hat{\mathbf{e}}_m$, $\hat{\mathbf{n}}_{nm}^h = \hat{\mathbf{h}}_n^+\hat{\mathbf{h}}_m$ and $\hat{\mathbf{p}}_{nm} = \hat{\mathbf{h}}_n\hat{\mathbf{e}}_m$ are mutually coupled as

$$\begin{aligned} i\frac{d}{dt}\hat{\mathbf{n}}_{nm}^e &= (\tilde{\varepsilon}_m^e - \tilde{\varepsilon}_n^e)\hat{\mathbf{n}}_{nm}^e - c_{m-1}^e\hat{\mathbf{n}}_{nm-1}^e - c_m^e\hat{\mathbf{n}}_{nm+1}^e + c_{n-1}^e\hat{\mathbf{n}}_{n-1m}^e + c_n^e\hat{\mathbf{n}}_{n+1m}^e + E(t)(d_m\hat{\mathbf{p}}_{mn}^+ - d_n\hat{\mathbf{p}}_{nm}), \\ i\frac{d}{dt}\hat{\mathbf{n}}_{nm}^h &= (\tilde{\varepsilon}_m^h - \tilde{\varepsilon}_n^h)\hat{\mathbf{n}}_{nm}^h - c_{m-1}^h\hat{\mathbf{n}}_{nm-1}^h - c_m^h\hat{\mathbf{n}}_{nm+1}^h + c_{n-1}^h\hat{\mathbf{n}}_{n-1m}^h + c_n^h\hat{\mathbf{n}}_{n+1m}^h + E(t)(d_m\hat{\mathbf{p}}_{mn}^+ - d_n\hat{\mathbf{p}}_{nm}), \\ i\frac{d}{dt}\hat{\mathbf{p}}_{nm} &= (\tilde{\varepsilon}_m^e + \tilde{\varepsilon}_n^h)\hat{\mathbf{p}}_{nm} - c_{m-1}^e\hat{\mathbf{p}}_{nm-1} - c_m^e\hat{\mathbf{p}}_{nm+1} - c_{n-1}^h\hat{\mathbf{p}}_{n-1m} - c_n^h\hat{\mathbf{p}}_{n+1m} + E(t)(d_m\delta_{nm} - d_n\hat{\mathbf{n}}_{nm}^e - d_m\hat{\mathbf{n}}_{mn}^h) \end{aligned}$$

C. Expectation values

In the Heisenberg picture time dependence is solely contained in the operators and the system remains in the initial or equilibrium state $|0\rangle$. Time-dependent expectation values of the polarization (28) and the intraband current (31) are, therefore, given inside the nanostructure by

$$\begin{aligned} P(t) &= \langle 0|\hat{\mathbf{P}}(t)|0\rangle = \sum_{n=-\infty}^{\infty} [d_n(\langle 0|\hat{\mathbf{p}}_{nn}^+|0\rangle^* + \langle 0|\hat{\mathbf{p}}_{nn}|0\rangle) + V_n(\langle 0|\hat{\mathbf{n}}_{nn}^h|0\rangle - \langle 0|\hat{\mathbf{n}}_{nn}^e|0\rangle)], \\ J(t) &= \langle 0|\hat{\mathbf{J}}(t)|0\rangle = \frac{a}{i} \sum_{n=-\infty}^{\infty} [c_n^h(\langle 0|\hat{\mathbf{n}}_{n+1}^h|0\rangle - \langle 0|\hat{\mathbf{n}}_{n-1}^h|0\rangle) - c_n^e(\langle 0|\hat{\mathbf{n}}_{n+1}^e|0\rangle - \langle 0|\hat{\mathbf{n}}_{n-1}^e|0\rangle)], \end{aligned} \quad (33)$$

where we have expressed effective masses by respective coupling constants. Note that in free space only free electrons can contribute to the current. Here the unit cell size a in Eq. (33) has to be replaced by dx corresponding to our free space discretization.

Radiation is generated by accelerated carriers and is proportional to the squared Fourier transform (FT) of the second derivative of the polarization and of the first derivative of the current as

$$S(\omega) \sim |\omega^2\text{FT}[P(t)](\omega) + i\omega\text{FT}[J(t)](\omega)|^2. \quad (34)$$

Also, intraband currents drive the optical field. In a one-dimensional k -space representation they are represented by [10,11]

$$\hat{\mathbf{J}}(t) = \int_{-\pi/a}^{\pi/a} dk [v_h(k)\hat{\mathbf{h}}_k^+\hat{\mathbf{h}}_k - v_e(k)\hat{\mathbf{e}}_k^+\hat{\mathbf{e}}_k] \quad (29)$$

with $v_{e/h}(k)$ being the group velocities of electrons and holes, which are defined by derivatives of the dispersion relation. For cosine shaped bands they are denoted by

$$v_{e/h}(k) = \frac{\partial}{\partial k}\varepsilon_{e/h}(k) = \frac{1}{m_{e/h}a} \sin(ak). \quad (30)$$

We now insert this expression into Eq. (29), apply transformation (15), and come to a space resolved expression for the operator of the current density as

$$\begin{aligned} \hat{\mathbf{J}}(t) &= \frac{1}{2ia} \sum_n \left[\frac{1}{m_h}(\hat{\mathbf{h}}_n^+\hat{\mathbf{h}}_{n+1} - \hat{\mathbf{h}}_n^+\hat{\mathbf{h}}_{n-1}) \right. \\ &\quad \left. - \frac{1}{m_e}(\hat{\mathbf{e}}_n^+\hat{\mathbf{e}}_{n+1} - \hat{\mathbf{e}}_n^+\hat{\mathbf{e}}_{n-1}) \right]. \end{aligned} \quad (31)$$

To determine P and J we must follow the evolution of expectation values of two-particle correlations, i.e.,

$$n_{nm}^e(t) = \langle 0 | \hat{\mathbf{n}}_{nm}^e | 0 \rangle, \quad (35)$$

$$n_{nm}^h(t) = \langle 0 | \hat{\mathbf{n}}_{nm}^h | 0 \rangle, \quad \text{and} \quad (36)$$

$$p_{nm}(t) = \langle 0 | \hat{\mathbf{p}}_{nm} | 0 \rangle. \quad (37)$$

Finally, the complete set of evolution equations required to determine the HHG spectrum (34) reads as

$$i \frac{d}{dt} n_{nm}^e = (\tilde{\varepsilon}_m^e - \tilde{\varepsilon}_n^e) n_{nm}^e - c_{m-1}^e n_{nm-1}^e - c_m^e n_{nm+1}^e + c_{n-1}^e n_{n-1m}^e + c_n^e n_{n+1m}^e + E(t)(d_m p_{mn}^* - d_n p_{nm}), \quad (38)$$

$$i \frac{d}{dt} n_{nm}^h = (\tilde{\varepsilon}_m^h - \tilde{\varepsilon}_n^h) n_{nm}^h - c_{m-1}^h n_{nm-1}^h - c_m^h n_{nm+1}^h + c_{n-1}^h n_{n-1m}^h + c_n^h n_{n+1m}^h + E(t)(d_m p_{mn}^* - d_n p_{nm}), \quad (39)$$

$$i \frac{d}{dt} p_{nm} = (\tilde{\varepsilon}_m^e + \tilde{\varepsilon}_n^h) p_{nm} - c_{m-1}^e p_{nm-1} - c_m^e p_{nm+1} - c_{n-1}^h p_{n-1m} - c_n^h p_{n+1m} + E(t)(d_m \delta_{nm} - d_n n_{nm}^e - d_m n_{mn}^h). \quad (40)$$

VII. DAMPING

The properties of real systems are critically determined by fast damping processes which go far beyond a two-particle description. In SBEs a phase relaxation time T_2 is introduced and ensures optical spectra with well-separated harmonic peaks with Lorentzian line shape [10, 11]. In order to introduce those relaxation times, we modify the on-site energies within the nanostructure according to $\tilde{\varepsilon}_n^e(t) = \varepsilon_n^e - \frac{i}{2T_2} + c_{n-1}^e + c_n^e - E(t)V_n$ and $\tilde{\varepsilon}_n^h(t) = \varepsilon_n^h - \frac{i}{2T_2} + c_{n-1}^h + c_n^h + E(t)V_n$. Note that such a change influences the evolution Eq. (40) of the polarization only, but not those of the carrier concentrations.

Also, intraband or Ohmic currents are damped with a characteristic time T_j . In momentum space such dissipative processes are described by a forced relaxation of carriers towards the bottom of respective bands.

According to Eq. (33) imaginary parts of off-diagonal elements $n_{nm-1}^{e/h}$ and $n_{nm+1}^{e/h}$ represent Ohmic currents in a

space-resolved representation. If those shall decay, a damping of these components via additional terms of the form $-\frac{1}{T_j}(n_{nm}^{e/h} - n_{mn}^{e/h})$ in Eqs. (38) and (39) must be added to the evolution equations inside the semiconductor. These damping terms become active only for pronounced asymmetries of respective two-particle correlation functions.

We assume damping to happen inside the nanostructure only, resulting in space dependent relaxation times as

$$T_n^{p/j} = \begin{cases} T_{2/j} & \text{inside the nanostructure for } |na - x_0| \leq L/2 \\ \infty & \text{in free space} \end{cases}.$$

Although such a description of relaxation phenomena is the simplest possible approach, respective relaxation times are not well known and vary considerably from system to system. Hence, a more involved treatment would also require a deeper investigation of relaxation of its own.

VIII. FINAL SET OF EVOLUTION EQUATIONS

The final set of evolution equations, which must be solved numerically, reads as

$$i \frac{d}{dt} n_{nm}^e = [\varepsilon_m^e - \varepsilon_n^e + c_{m-1}^e + c_m^e - c_{n-1}^e - c_n^e - E(t)(V_m - V_n)] n_{nm}^e - \frac{i}{2} \left(\frac{1}{T_n^j} + \frac{1}{T_m^j} \right) (n_{nm}^e - n_{mn}^e) - c_{m-1}^e n_{nm-1}^e - c_m^e n_{nm+1}^e + c_{n-1}^e n_{n-1m}^e + c_n^e n_{n+1m}^e + E(t)(d_m p_{mn}^* - d_n p_{nm}), \quad (41)$$

$$i \frac{d}{dt} n_{nm}^h = [\varepsilon_m^h - \varepsilon_n^h + c_{m-1}^h + c_m^h - c_{n-1}^h - c_n^h + E(t)(V_m - V_n)] n_{nm}^h - \frac{i}{2} \left(\frac{1}{T_n^j} + \frac{1}{T_m^j} \right) (n_{nm}^h - n_{mn}^h) - c_{m-1}^h n_{nm-1}^h - c_m^h n_{nm+1}^h + c_{n-1}^h n_{n-1m}^h + c_n^h n_{n+1m}^h + E(t)(d_m p_{mn}^* - d_n p_{nm}), \quad (42)$$

$$i \frac{d}{dt} p_{nm} = \left[\varepsilon_m^e + \varepsilon_n^h - \frac{i}{2} \left(\frac{1}{T_n^p} + \frac{1}{T_m^p} \right) + E(t)(V_n - V_m) + c_{m-1}^e + c_m^e + c_{n-1}^h + c_n^h \right] p_{nm} - c_{m-1}^e p_{nm-1} - c_m^e p_{nm+1} - c_{n-1}^h p_{n-1m} - c_n^h p_{n+1m} + E(t)(d_m \delta_{nm} - d_n n_{nm}^e - d_m n_{mn}^h). \quad (43)$$

Here, all computed quantities, namely n_{nm}^e , n_{nm}^h , and p_{nm} , vanish before the arrival of the pulse.

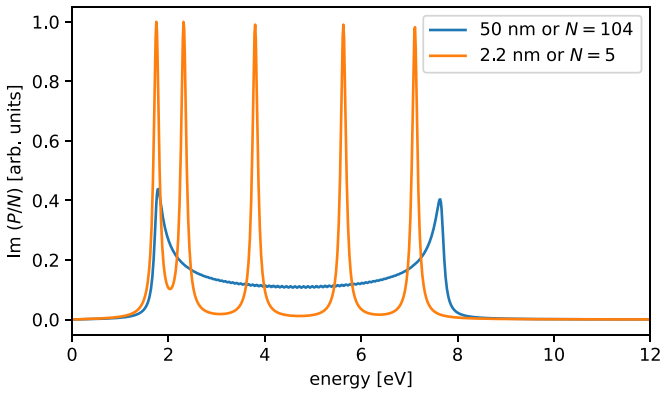


FIG. 3. Linear optical properties of nanostructures under investigation. Imaginary parts of polarizability per site are displayed for a large bulklike nanowire and a small one, for which quantum confinement plays an essential role (for parameters see Appendix).

IX. NUMERICAL RESULTS: HHG IN A CdSe NANOSTRUCTURE

Here, we study HHG in nanostructures made from CdSe, one of the standard systems to produce semiconductor quantum dots with tunable size by chemical synthesis (see [22] and references therein). Its bulk material parameters are well known (see the Appendix) and very recently, CdSe quantum dots have been experimentally examined in the context of HHG [16]. Surprisingly, HHG was found to be suppressed for smaller dots compared with the bulk material.

As already pointed out in the Introduction, full *ab initio* approaches to model this system are computationally prohibitive and the here developed theoretical approach is required to make a reliable modeling.

The above-derived set of Eqs. (41)–(43) is capable of describing the optical response of a semiconductor nanostructure within the limits set by the underlying approximations. We numerically solve these equations using a home-made code in C++, in which numerical integration of the differential Eqs. (41)–(43) is performed based on a standard adaptive Runge-Kutta scheme [23] (for a public available version of our code, see [24]).

We investigate different quantum wires, between 2.2 and 50 nm in length containing between 5 and 104 unit cells, respectively. Modeling of a nanostructure of 2.2 nm length embedded in 15 nm of surrounding space and excited by a 100-fs pulse as in typical experiments reported in [16] required less than 10 s on a workstation (Intel Xenon, 8 GB RAM). Although respective calculations are orders of magnitude faster, both quantum confinement and the linear optical response of semiconducting nanostructures are reproduced.

To probe the linear spectral response, we excite the system with a weak delta-like pulse (nonoscillating Gaussian shape, centered at $t = 0$, $W_{\text{FWHM}} = 0.1$ fs, peak amplitude 0.001 V/nm) and follow the evolution of the microscopic expectation values (41)–(43). As soon as the current J is negligible, the resulting polarization, Eq. (33), is Fourier-transformed to obtain the complex linear polarizability p . The imaginary part of this polarizability, as displayed in Fig. 3 per site, is linked to linear absorption. Not surprisingly, the 50-nm wire (blue line) behaves like a one-dimensional bulk solid, featuring a

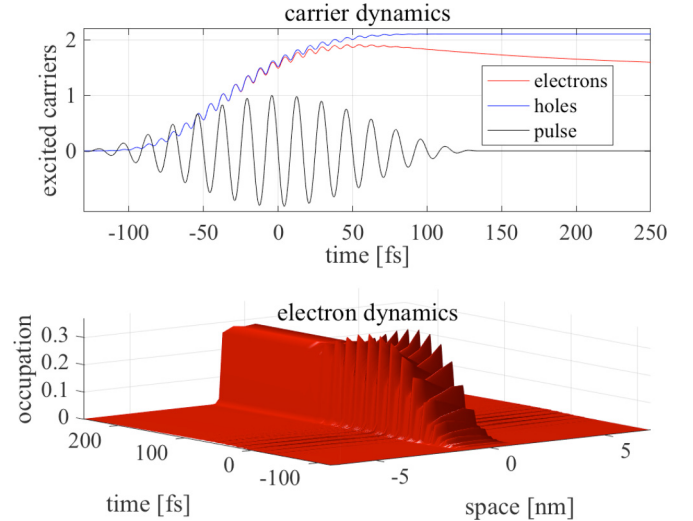


FIG. 4. Evolution of carrier numbers and occupation of individual sites in an optically excited nanowire of 2.2 nm length (five sites). Electrons are emitted to free space resulting in an overall loss of carriers. Additionally, the optical field of the exciting pulse is displayed for comparison. Pulse duration: 100 fs; carrier wavelength: 5 μm ; field strength: 2.5 V/nm in free space; polarization: linear along the wire.

broad quasistuctureless absorption band (blue line), which is spectrally limited to the spectral range of the interband transition between the two cosine-shaped bands. We also see the typical enhancement at the band edge as expected for a one-dimensional structure. Due to the absence of Coulomb interaction in our model, the otherwise well-pronounced excitation peak is missing. In contrast, the linear optical response of the 2.2 nm structure (red line) is determined by quantum confinement causing the spectrum to be structured with localized absorption features corresponding to the number of real-space sites involved.

After having validated the linear optical properties, we next investigate the systems' nonlinear optical response. Interaction with intense optical pulses (carrier wavelength 4000 nm, $W_{\text{FWHM}} = 100$ fs, peak amplitude in free space 2.5 V/nm) results in complex carrier dynamics including the excitation of electrons and holes as displayed for the tiny wire (2.2 nm length or five sites) in Fig. 4. The evolution is dominated by Rabi oscillations, but due to the finite relaxation times ($T_2 = T_1 = 10$ fs), a net generation of carriers occurs so that electrons and holes remain after the pulse has passed. As already predicted on the basis of a solution of the TDSE (see Fig. 1) excited electrons are further accelerated by the optical field causing even a weak emission to free space and consequently a loss of electrons. In what follows, we will investigate how these complex joint dynamics of electrons and holes affects HHG.

We first model HHG for the large (50 nm) and the tiny (2.2 nm) wire, where we expect bulk behavior for the first and confinement effects for the second system (see Fig. 5). Indeed, the spectra of the large wire (blue line) are like those obtained on the basis of SBEs for bulk semiconductors [7,10]. We identify the characteristic plateau region, which stretches from the band gap (1.75 eV) up to the maximum possible

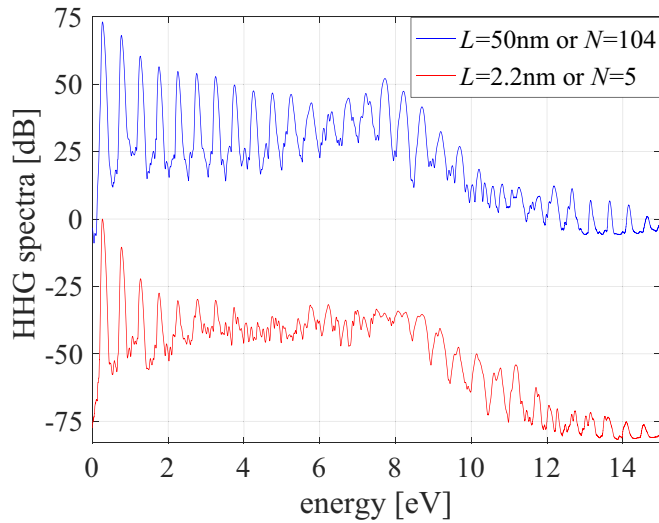


FIG. 5. Influence of confinement on HHG spectra. The spectra are generated by an intense pulse in a large bulklike nanowire (blue line) and a small one (red line), for which quantum confinement plays an essential role. Parameters as in Fig. 4. The spectra are scaled by the squared number of sites. The blue line is shifted by +75 dB for better visibility.

energy of an interband transition (within our model roughly 8 eV). In contrast, the HHG spectrum of the tiny structure is obviously strongly affected by confinement. It is orders of magnitude weaker and noticeably distorted compared with the bulk spectrum. Even if divided by the squared number of sites to compensate for the coherent enhancement, the power in almost all harmonic orders of the large structure (104 sites) is considerably higher than that emitted by the tiny (five sites) wire. Moreover, the harmonic orders of the tiny structure also drop off much quicker such that already the seventh order is more than 300 times weaker than the first one. In the case of the large structure, only the harmonics starting from the 17th order (above 4 eV) are comparably reduced.

Taken together, two reasons for this modification of HHG in nanostructures can be identified: On the one hand, there is a considerable change of the energetic structure, which not only affects the linear optical properties (see Fig. 3). On the other hand, in tiny nanostructures, electrons, and holes constantly interact with the interface, an effect which is also missing in the bulk. Our model allows us to disentangle these two contributions.

First, we mimic complete confinement by increasing the free space energy $\varepsilon_{\text{free space}}$ in Eq. (22) to a quasi-infinite value (increase by a factor of 6). This immediately causes a further dropoff of HHG spectra as demonstrated in Fig. 6 (lower black line). Hence, much higher energetic walls impede HHG considerably. Thus, we can assign this to be the predominant reason for the lower yield of the tiny wire. The overall reduction of HHG is even stronger than in a nanostructure with realistic walls (cf. black and red lines in Fig. 6). Consequently, the properties of the boundaries, which are constantly probed by accelerated carriers have a strong impact on HHG in nanostructures.

For a finite binding potential, the spatial shape of the wave function is not considerably changed compared with

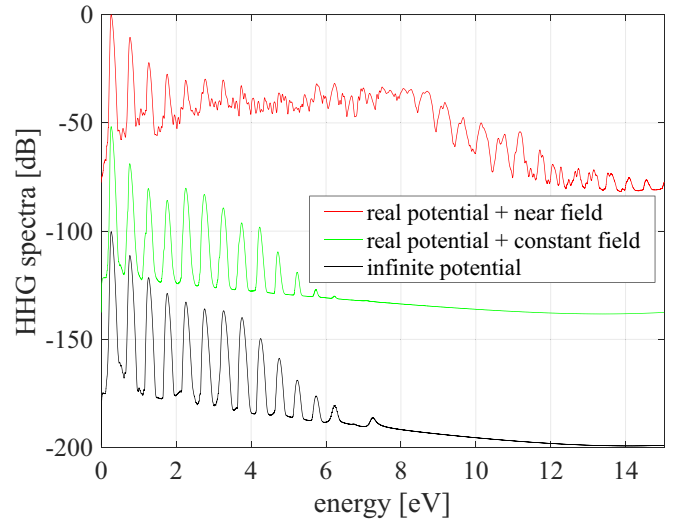


FIG. 6. Influence of the embedding environment on the HHG spectrum of a tiny nanostructures (five sites or 2.2 nm). Spectra of nanostructures with different confinement potentials and surrounding field structure are displayed (parameters as in Fig. 4). The green and the black line are shifted by -50 and -100 dB, respectively.

the eigenstates of a box potential. But electrons may exit into free space when driven by the electric field (cf. Fig. 4). Emitted electrons experience the optical near field which can be considerably stronger than the electrical field inside the semiconductor [for a sphere, see Eq. (26)]. To quantify this effect, we assume that the dielectric constant of the space surrounding the nanostructure coincides with that of the semiconductor. This keeps the optical field in the surrounding space constant at its bulk value within the entire simulation domain. Such homogenization of the electrical field has again a pronounced negative effect on HHG as demonstrated in Fig. 6 (green line). We do not only observe a strong reduction of yield, but also a considerably reduced cutoff of the spectrum. Consequently, we conclude that the near-field enhancement amplifies HHG. Thus, optically accelerated electrons can be used to probe electrical near fields thereby connecting the wire's quantum dynamics with electrodynamics.

Periodically driven particles that interact with boundaries tend to move chaotically, as is well known from classical mechanics. In our nanostructure, this behavior is partially suppressed by damping, a feature which we have included into our simulations via the finite phase relaxation time T_2 and the finite intraband current damping time T_j [see Eqs. (41)–(43)]. Still, traces of the irregular motion are seen, e.g., in the evolution of the center of gravity of our carrier distribution. They become more apparent if we completely switch off the damping of the interband currents (compare the upper left and right parts of Fig. 7).

The interplay of such quasichaotic behavior and damping has a profound impact on HHG (see the lower plot of Fig. 7). If all relaxation times are set to infinity, Rabi oscillations prevail, and all carriers are periodically generated and completely reabsorbed. A few discrete higher harmonics can still be found (see blue curve in the lower plot of Fig. 7), but carrier motion

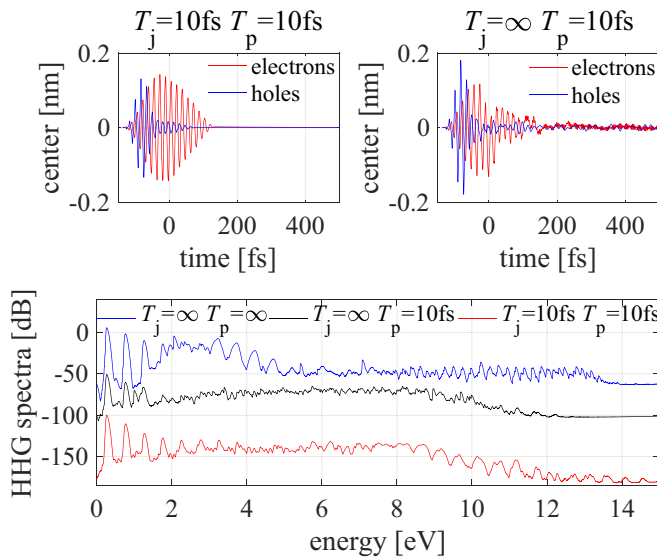


FIG. 7. Influence of damping on the carrier evolution (upper row) and HHG (lower graph) in a nanostructure (five sites or 2.2 nm). The black and the red line in the lower graph are shifted by -50 and -100 dB, respectively.

and all frequency components generated by it are missing. This changes if dephasing is added so that electrons and holes are continuously generated. Due to the ongoing field-induced acceleration and the interaction with the interfaces, these carriers undergo a quasichaotic motion and, in consequence, a large plateau of newly generated frequencies emerges (see black plateau in lower plot of Fig. 7). Damping of interband currents again quenches this quasichaotic motion (compare the two upper plots of Fig. 7), but now regular spectral peaks evolve (see red line in the lower plot of Fig. 7).

Our tight-binding approach also enables us to study the influence of structural defects and lattice distortions on HHG in more detail. Here we investigate effects of surface relaxation of a 5-nm structure (11 sites) and assume that the outer and second most outer unit cells are displaced by 20% and 10% of the unit cell length inwards, resulting in an overall diameter reduction of 1.4 Å. These are typical values obtained from stationary solutions of the eigenvalue equation of such structures within DFT or XTb approaches; see Fig. 2. Consequently, the coupling strength is increased by 44% and 21% according to the Harrison scaling [25]. The imaginary part of the linear polarizability is calculated similarly as it was done for the spectra displayed in Fig. 3. A clearly visible surface state appears at the upper edge of the absorption spectrum (see Fig. 8). Again, HHG was calculated for a 50 fs Gaussian pulse with a wavelength of 5000 nm and maximum field strength of 1.5 V/nm. In contrast to the linear response, HHG seems not to be significantly affected by the newly emerged localized surface states.

X. SUMMARY AND CONCLUSIONS

In conclusion, we have transferred the successful approach of SBEs to describe HHG in bulk matter from reciprocal to real space using a tight-binding approach. We describe

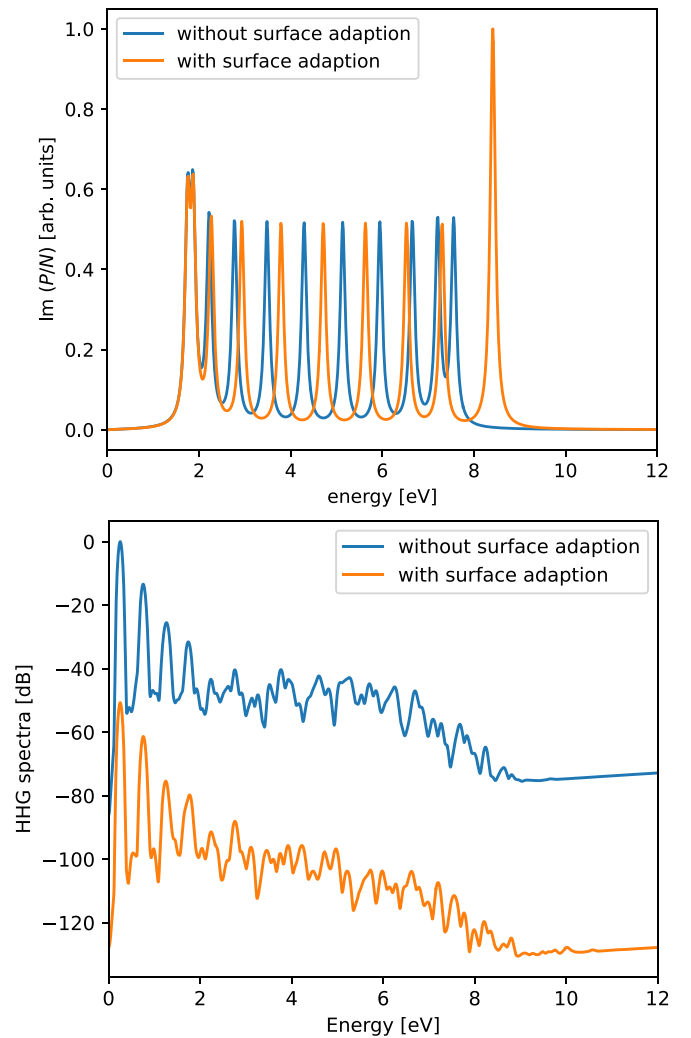


FIG. 8. Influence of surface adaption on linear absorption (upper graph) and HHG (lower graph) in a nanostructure (11 sites or 5 nm). In case of surface adaption (orange line) the outer and second most outer unit cells are displaced by 20% and 10% of the unit cell length inwards, respectively.

intense-field-driven semiconductor nanostructures with the same precision as the bulk material and based on the knowledge of bulk properties as gap energies, effective masses, and dipole elements. Thus, we gain detailed insight into the field-driven electron-hole dynamics and the evolution of two-particle correlations of finite systems, in particular, in the vicinity of interfaces. In our approach, the electrons may even leave the nanostructure leading to ionization, can possibly return, may be affected by an inhomogeneous nearfield in the vicinity of the dot, and may interact with holes remaining inside the dot. The impact of these effects on the nonlinear dynamics and the corresponding nonlinear response can be analyzed separately.

Here, we have applied our approach to selected science cases—a one-dimensional two-band nanoscale semiconductor embedded in free space that interacts with a strong light field and generates higher-order harmonic radiation. We have shown that quantum confinement reduces the HHG efficiency in accordance with newly published experimental

results [16]. But, the interaction between the excited carriers and the boundaries also leaves significant traces in the higher-harmonic spectra. Accelerated and partially transmitted electrons constantly probe the optical near field around the nanostructure leading to emitted spectra, which depend on the strength of the field enhancement around the nanoparticle. Moreover, we also have incorporated different possible relaxation phenomena, specifically phase relaxation and damping of intraband currents. The shape and extent of the generated spectra depend sensitively on the choice of respective relaxation times.

Although we have demonstrated our scheme for a simple one-dimensional case only, it is straightforward to extend it into various directions. Three-dimensional objects consisting of semiconductors with many, and potentially anisotropic, bands can be incorporated using tight-binding parameters derived from state-of-the-art DFT codes. As the carrier evolution in each unit cell of the semiconductor crystal is represented by a few complex numbers only, the resulting growth of numerical complexity can still be handled. Even for three-dimensional structures it will be considerably lower than that required for standard time dependent DFT calculations. It must be emphasized that our approach can incorporate quasi-particles consisting of pairs of particles such as excitons. In the present work, we have not included these excitonic effects yet as the applied optical fields have been much stronger than the expected internal forces that would form the excitons. Nonetheless, an inclusion of Coulomb interaction into our framework is straightforward and would not increase the complexity of our code considerably.

In general, our code is well suited for the space and time resolved description of electron and hole dynamics in nanostructured crystallin solids, particularly if bulk properties are well known and respective nanostructures are too big to be treated with *ab initio* methods. Beyond the above mentioned HHG in quantum dots [16], typical examples are the modeling of electron hole dynamics in finite flakes of two-dimensional materials [26], the simulation of hot carrier dynamics at plasmonic interfaces [27], and the interaction between light driven electrons and attached molecules in tip enhanced Raman spectroscopy [28].

ACKNOWLEDGMENT

We acknowledge funding by the DFG in the framework of SFB 1375 NOA.

APPENDIX

1. Parameters of a CdSe quantum dot used in simulations

Unless otherwise stated material parameters are taken from [29].

(i) Size of the unit cell of CdSe (wurtzite):

$$\begin{aligned}\tilde{a} &= 4.3\text{Å}, \quad \tilde{c} = 7\text{Å} \Rightarrow \tilde{a} = \sqrt[3]{\tilde{a}^2\tilde{c}} \\ &= 4.8\text{Å normalized } a = 9.057.\end{aligned}$$

(ii) Coupling:

electrons inside the dot $m_e = 0.13 \Rightarrow c_n^e = \frac{1}{2a^2m_e} = 0.04689$,

electrons in free space: $c_n^e = \frac{1}{2dx^2}$ with dx : space discretization in normalized units,

holes inside the dot: $m_h \approx 0.8 \Rightarrow c_n^h = \frac{1}{2a^2m_h} = 0.00762$.

(iii) Energies:

gap: $E_{\text{gap}} = 1.75 \text{ eV} \Rightarrow \varepsilon_{\text{gap}} = 0.063$,

free space: $E_{\text{valence band}} = -6.69 \text{ eV} \Rightarrow \varepsilon_{\text{free space}} = \frac{-E_{\text{gap}}/2 - E_{\text{valence band}}}{E_{\text{Hartree}}} = 0.214$.

(iv) Dipole matrix elements:

momentum matrix element: $\langle p_k \rangle = \int_{-a/2}^{a/2} dx u_k^{c*}(x) \frac{1}{i} \frac{\partial}{\partial x} u_k^v(x)$,
 $\frac{2}{m_0} \langle p_k \rangle^2 = 20 \text{ eV}$ (according to [30]),

$$\tilde{d} \approx \frac{\hbar}{m_0 E_{\text{gap}}} \langle \tilde{p} \rangle = 5 \text{ Å} \Rightarrow D_0 \approx 9.4.$$

(v) Relative dielectric constant:

inside the dot, $\varepsilon_{\text{CdSe}}^R \approx 6$,

outside, $\varepsilon_{\text{free space}}^R = 1$.

2. Calculation of HHG spectra

Polarizations and currents are determined according to Eq. (33) during each time step. Computations are continued until all interband polarizations and interband currents have decayed [usually three times the pulse width, full width at half maximum (FWHM)]. The final time dependent data files were artificially extended to 20 times their original length by zero-padding in order to increase the frequency resolution. Then, the spectral intensity was determined according to Eq. (34). Finally, fast oscillations of this power spectrum were filtered out by making a convolution with a Gaussian filter function with a width of a fifth of the fundamental frequency, thus simulating a spectrometer with a limited spectral resolution.

3. Time-dependent Schrödinger equation

We numerically solve the time-dependent Schrödinger equation (TDSE) for a single-active electron on a one-dimensional grid using the split-operator [31]. The grid ranged, for the smallest here investigated system, $[-20 \text{ nm}; 20 \text{ nm}]$, employing 4096 grid points. The model potential is given by

$$V(x) = \begin{cases} -V_0, & |x| \leq d/2 \\ \frac{q}{\sqrt{(x-d/2)^2 + \frac{q^2}{V_0^2}}}, & |x| > d/2, \text{ with } V_0 = 6.7 \text{ eV}, q = 1, \\ \text{and } d = 2.2 \text{ nm.} \end{cases}$$

Eigenstates are obtained by the imaginary time propagation. The time steps are $\Delta t = 0.01 \text{ fs}$. Interaction is given in length gauge employing a laser field as defined above, employing the following pulse parameters: max field strength: 2.5 V/nm; wavelength: 5000 nm; pulse shape: Gaussian with FWHM 100 fs. The HHG spectra are obtained from the Fourier transform of the dipole acceleration. Results are given in Fig. 1. The total computational time is roughly 10 s.

4. Real-time time-dependent density functional theory

We have performed full real-time time-dependent density functional theory (rtTDDFT) simulation of such a nanos-

structure composed of 4, 16, and 64 atoms, respectively, employing the package OCTOPUS [17]. The only feasible exchange-correlation functional is the LDA functional [32,33]. For the calculations two electrons per atom were included explicitly. The effect of the other electrons was incorporated for by pseudopotentials [34]. The spherical simulation box had a radius of 18 Å with an imaginary absorber of 2.7 Å. The pulse was defined to be a \sin^2 envelope with a full width at half maximum (FWHM) of 50 fs, a peak intensity of 1.2×10^{11} W/cm² (corresponding to

a field strength of 9.95 V/nm), and a wavelength of 3800 nm. Time steps are defined to be 0.25 atomic units. The harmonic spectra were obtained from the total charge current $\mathbf{J}(\mathbf{r}, t)$ as

$$S(\omega) \sim \omega^2 \left| \int \mathbf{J}(\mathbf{r}, t) e^{-i\omega t} \right|^2.$$

The calculations required more than 175 000 CPU hours for the 64-atom dot (1.6 nm size). The corresponding results are shown in Fig. 2.

-
- [1] S. Ghimire, A. D. DiChiara, E. Sistrunk, P. Agostini, L. F. DiMauro, and D. A. Reis, Observation of high-order harmonic generation in a bulk crystal, *Nat. Phys.* **7**, 138 (2011).
- [2] G. Vampa, T. J. Hammond, N. Thiré, B. E. Schmidt, F. Légaré, C. R. McDonald, T. Brabec, D. D. Klug, and P. B. Corkum, All-Optical Reconstruction of Crystal Band Structure, *Phys. Rev. Lett.* **115**, 193603 (2015).
- [3] E. A. Stepanov, A. B. Fedotov, and A. M. Zheltikov, Mapping the electron band structure by intraband high-harmonic generation in solids, *Optica* **4**, 516 (2017).
- [4] O. Schubert, M. Hohenleutner, F. Langer, B. Urbanek, C. Lange, U. Huttner, D. Golde, T. Meier, M. Kira, S. W. Koch, and R. Huber, Sub-cycle control of terahertz high-harmonic generation by dynamical Bloch oscillations, *Nat. Photon.* **8**, 119 (2014).
- [5] T. T. Luu, M. Garg, S. Y. Kruchinin, A. Moulet, M. T. Hassan, and E. Goulielmakis, Extreme ultraviolet high-harmonic spectroscopy of solids, *Nature (London)* **521**, 498 (2015).
- [6] D. Bauer and K. K. Hansen, High-Harmonic Generation in Solids with and without Topological Edge States, *Phys. Rev. Lett.* **120**, 177401 (2018).
- [7] C. R. McDonald, G. Vampa, P. B. Corkum, and T. Brabec, Interband Bloch oscillation mechanism for high-harmonic generation in semiconductor crystals, *Phys. Rev. A* **92**, 033845 (2015).
- [8] M. Korbman, S. Y. Kruchinin, and V. S. Yakovlev, Quantum beats in the polarization response of a dielectric to intense few-cycle laser pulses, *New J. Phys.* **15**, 013006 (2013).
- [9] N. Tancogne-Dejean, O. D. Mücke, F. X. Kärtner, and A. Rubio, Ellipticity dependence of high-harmonic generation in solids originating from coupled intraband and interband dynamics, *Nat. Commun.* **8**, 745 (2017).
- [10] D. Golde, T. Meier, and S. W. Koch, High harmonics generated in semiconductor nanostructures by the coupled dynamics of optical inter- and intraband excitations, *Phys. Rev. B* **77**, 075330 (2008).
- [11] M. Kira and S. W. Koch, *Semiconductor Quantum Optics* (Cambridge University Press, Cambridge, UK, 2012).
- [12] S. Almalki, A. M. Parks, G. Bart, P. B. Corkum, T. Brabec, and C. R. McDonald, High harmonic generation tomography of impurities in solids: Conceptual analysis, *Phys. Rev. B* **98**, 144307 (2018).
- [13] G. Orlando, C.-M. Wang, T.-S. Ho, and S.-I. Chu, High-order harmonic generation in disordered semiconductors, *J. Opt. Soc. Am. B* **35**, 680 (2018).
- [14] G. Orlando, T.-S. Ho, and S.-I. Chu, Simple model of dephasing for high-order harmonic generation in solids, *J. Opt. Soc. Am. B* **37**, 1540 (2020).
- [15] C. R. McDonald, K. S. Amin, S. Aalmalki, and T. Brabec, Enhancing High Harmonic Output in Solids Through Quantum Confinement, *Phys. Rev. Lett.* **119**, 183902 (2017).
- [16] K. Nakagawa, H. Hirori, S. A. Sato, H. Tahara, F. Sekiguchi, G. Yumoto, M. Saruyama, R. Sato, T. Teranishi, and Y. Kanemitsu, Size-controlled quantum dots reveal the impact of intraband transitions on high-order harmonic generation in solids, *Nat. Phys.* **18**, 874 (2022).
- [17] https://octopus-code.org/wiki/Main_Page.
- [18] R. E. F. Silva, F. Martín, and M. Ivanov, High harmonic generation in crystals using maximally localized Wannier functions, *Phys. Rev. B* **100**, 195201 (2019).
- [19] M. G. Burt, The evaluation of the matrix element for interband optical transitions in quantum wells using envelope functions, *J. Phys.: Condens. Matter* **5**, 4091 (1993).
- [20] B. Gu, N. H. Kwong, and R. Binder, Relation between the interband dipole and momentum matrix elements in semiconductors, *Phys. Rev. B* **87**, 125301 (2013).
- [21] J. D. Jackson, in *Classical Electrodynamics*, 3rd ed. (John Wiley & Sons, New York, 1998), p. 184, Eq. 4.54.
- [22] V. Singh, P. V. More Priyanka, E. Hemmer, Y. K. Mishra, and P. K. Khanna, Magic-sized CdSe nanoclusters: A review on synthesis, properties and white light potential, *Mater. Adv.* **2**, 1204 (2021).
- [23] J. R. Dormand and P. J. Prince, A family of embedded Runge-Kutta formulae, *J. Comp. Appl. Math.* **6**, 19 (1980).
- [24] Our code: <https://gitlab.com/theoretical-chemistry-jena/strong-field-physics/nanostructure-1d-tb-hhg>.
- [25] W. A. Harrison, *Electronic Structure and Properties of Solids* (Freeman, San Francisco, 1980).
- [26] G. Fiori, F. Bonaccorso, G. Iannaccone, T. Palacios, D. Neumaier, A. Seabaugh, S. K. Banerjee, and L. Colombo, Electronics based on two-dimensional materials, *Nat. Nanotechnol.* **9**, 768 (2014).
- [27] M. Brongersma, N. Halas, and P. Nordlander, Plasmon-induced hot carrier science and technology, *Nat. Nanotechnol.* **10**, 25 (2015).
- [28] R. B. Jaculbia *et al.*, Single-molecule resonance Raman effect in a plasmonic nanocavity, *Nat. Nanotechnol.* **15**, 105 (2020).
- [29] E. Menendez-Proupin and C. Trallero-Giner, Electric-field and exciton structure in CdSe nanocrystals, *Phys. Rev. B* **69**, 125336 (2004).

- [30] C. Hermann and C. Weisbuch, $\vec{k} \cdot \vec{p}$ perturbation theory in III-V compounds and alloys: A reexamination, *Phys. Rev. B* **15**, 823 (1977).
- [31] M. D. Feit, J. A. Fleck, and A. Steiger, Solution of the Schrödinger equation by a spectral method, *J. Comput. Phys.* **47**, 412 (1982); R. Kosloff and H. Tal-Ezer, A direct relaxation method for calculating eigenfunctions and eigenvalues of the Schrödinger equation on a grid, *Chem. Phys. Lett.* **127**, 223 (1986).
- [32] P. A. M. Dirac, Note on exchange phenomena in the thomas atom, *Math. Proc. Cambridge Philos. Soc.* **26**, 376 (1930).
- [33] S. H. Vosko, L. Wilk, and M. Nusair, Accurate spin-dependent electron liquid correlation energies for local spin density calculations: A critical analysis, *Can. J. Phys.* **58**, 1200 (1980).
- [34] C. Hartwigsen, S. Goedecker, and J. Hutter, Relativistic separable dual-space Gaussian pseudopotentials, *Phys. Rev. B* **58**, 3641 (1998).